ORIGINAL RESEARCH ARTICLE

Puppet Strings of Hydrogen Plasma Reduction of Iron Ores: The Impact of Process Parameters on Plasma Properties and Reduction Kinetics

ANNA SHELYUG, HENRI PAUNA, HAUKE SPRINGER, and ISNALDI R. SOUZA FILHO

The reduction effect of plasma in the arc reactor under varying pressure (300–900 mbar), arc current (100–300 A), and electrode-to-sample distances (5–20 mm) was studied utilizing magnetite (Fe_3O_4) as a model material. Thermodynamic modeling and experimental results revealed that higher pressures improved metallic yield by reducing iron evaporation, achieving up to 89.4 pct reduction at 900 mbar. Kinetic analysis demonstrated rapid magnetite reduction to wüstite within the first 5 minutes and stabilization of metallic iron formation after 15 minutes, with higher currents expediting reduction but increasing energy demand. Plasma characterization via optical emission spectroscopy confirmed the hydrogen utilization efficiency by studying effects of Fe, H, Ar, and Na emissions on plasma behavior and process dynamics, including phenomena like double arcing and contamination from crucible materials. Energetic efficiency peaked at 900 mbar, 200 A, and 10 mm ACD, balancing metal yield and energy consumption.

https://doi.org/10.1007/s11663-025-03698-2

I. INTRODUCTION

In recent years, intensive research efforts have focused on harnessing hydrogen (H_2) as a clean and efficient reducing agent in metallurgical processes,[1,2] driven by the need to decarbonize the industry that is currently dominated by CO_2-intensive routes like the blast furnace and basic oxygen furnace integrated process (BF-BOF).[3] Among the alternative options, hydrogen-based direct reduction (HyDR) and hydrogen plasma smelting reduction (HPSR) have emerged as promising pathways for lowering the environmental footprint of metal extraction. HyDR employs H_2-containing gas mixtures to directly reduce iron oxides at moderate temperatures (800 °C–1000 °C),[4] while HPSR enables simultaneous melting and reduction of ore through the formation of highly reactive hydrogen plasma species (*e.g.,* H, H^+), enhancing both reaction kinetics and process integration.[5,6] When combined with electric arc furnaces (EAF), HPSR has the potential to achieve up to 80 pct CO_2 emission reductions compared to conventional primary steelmaking (IEA Report, 2022), representing a transformative step toward greener metallurgy.

One of HPSR's most compelling advantages lies in its operational flexibility, offering the ability to finely tune a range of process parameters—such as gas composition, pressure, arc length, and electrode configuration—almost like manipulating puppet strings to control a complex yet responsive system.[8–10] This high degree of tunability allows researchers and engineers to adapt the process to diverse feedstocks and production goals. However, despite this potential, significant knowledge gaps remain regarding how plasma characteristics—particularly shape, temperature, and electron pressure—govern reduction kinetics and overall process efficiency. Theoretical studies have suggested that electrode-sample distance and current intensity influence plasma stability and reactivity,[11] but a deeper understanding of ionic species distribution in different plasma environments is still evolving.

ANNA SHELYUG is with the Max-Planck Institute for Sustainable Materials, 40237 Düsseldorf, Germany and also with the Institute for Nuclear Waste Disposal, Karlsruhe Institute of Technology, 76344 Eggenstein-Leopoldshafen, Germany. Contact e-mail: anna.shelyug@kit.edu HENRI PAUNA is with the Process Metallurgy Research Unit, University of Oulu, P.O. Box 4300, 90014 Oulu, Finland. Contact e-mail: Henri.Pauna@oulu.fi HAUKE SPRINGER is with the Max-Planck Institute for Sustainable Materials and also with the Chair of Sustainable Metallurgy, Universität Duisburg-Essen 47119, Duisburg, Germany. ISNALDI R. SOUZA FILHO is with the Max-Planck Institute for Sustainable Materials and also with the Institut Jean Lamour, CNRS (UMR 7198), Université de Lorraine, 54000 Nancy, France.

Manuscript submitted April 14, 2025; accepted June 29, 2025.

To address these gaps, this study systematically investigates the influence of controllable HPSR parameters using magnetite (Fe_3O_4) as a reference material. By varying absolute pressure, arc length, and current magnitude under controlled conditions, we aim to reveal how each "string" in this plasma-based system can be adjusted to optimize hydrogen utilization and energy input. In doing so, the findings contribute not only to the development of sustainable ironmaking practices but also to the broader field of high-temperature hydrogen metallurgy, informing future reactor designs and reinforcing the case for environmentally conscious process innovation.

II. MATERIALS AND METHODS

A. *Material*

Magnetite fines (Fe_3O_4, Alfa Aesar, 97 pct metal basis) were used as a model material due to its thermal stability (viz., lack of thermal decomposition) under the experimental conditions of the current work (viz. low O_2 partial pressures and temperatures above 1600 °C). The corresponding chemical composition was assessed by mass spectrometry (MS) with inductively coupled plasma (ICP) and documented in Table I.

B. *Reduction Experiments*

The original magnetite powder was pre-compacted under a pressure of 1×10^7 Pa using a hydraulic press to avoid spatter and mass loss upon ignition of the arc. Pre-compacted green magnetite pellets of approximately 15 g total mass were placed onto water-cooled copper hearth (anode), as shown in the schematic representation of the furnace displayed in Figure 1(a).[6,12] The anode is placed immediately underneath the tungsten cathode (Figure 1) whose aspect ratio between its diameter and height is 6.34 mm/9.00 mm. The "anode-cathode distance" can be seen in Figure 1a and hereafter it is referred to as ACD. Different ACD values were investigated in this work, namely, 5, 10, 15, or 20 mm.

For the reduction experiments, the chamber of the furnace was evacuated to 1×10^{-4} bar, then filled with the gas mixture of Ar-10 pct H_2 to a desired absolute pressure of 300, 600, or 900 mbar [Figure 1(a)]. The strategy of decreasing the absolute pressure of the system permits enhancing the concentration of plasma species at lower temperatures, as studied in.[10] The electric arc was ignited at the edge of copper hearth, set to a desired current of 100, 200, or 300 A and then moved toward the sample to simultaneously melt and reduce it for 1 minutes. After the 1 minutes-melting was completed, the arc was switched off, the chamber evacuated and refilled again accordingly, thus completing one "experimental cycle." The cycles were repeated for the 0.5, 1, 5, 10, and 15 times and throughout the study the notation of minutes was used.

To investigate the impact of distinct process parameters on the plasma properties and reduction kinetics, systematic alterations were made to the absolute pressure of the system, the applied current, and the ACD values, as outlined in Figure 1(b), which provides a visual representation of the experimental matrix adopted in this work. In each experimental grouping, two parameters were held constant, while the third was systematically altered. Initially, a current of 200 A and an ACD value of 10 mm were established as the baseline.[6] Subsequently, the pressure was adjusted to 900 mbar, while retaining the 10 mm electrodes distance. In the final configuration, the pressure was again set to 900 mbar, this time alongside a current of 200 A. This meticulous arrangement yielded three distinct experimental sets, each comprising five samples. For each set of experiments, the duration of hydrogen plasma exposure was 0.5, 1, 5, 10, and 15 minutes.

For each experiment, the values of the input energy were recorded as of absolute values before and after each experiment. After the reduction process, the rapidly solidified samples were weighed and crushed to separate the remaining unreduced oxide portions from metallic iron pieces, which were also weighed separately.

C. *Phase Composition and Microstructural Analysis*

The phase composition of the powdered portions was inferred by X-Ray Diffraction (XRD), performed on a Bruker D8 Advance A25 X1 with Bragg Brentano geometry, and equipped with a CoK_α (λ = 1.78897 Å) source. The XRD scans were recorded in the diffraction angle 2θ range between 20 and 130 deg, using a step size of 0.009 deg and 224.64 s/step signal collection. Rietveld refinement was employed to estimate the weight fraction of the constituents in the powder using the MDI Jade v8.6 software with coupled with the PDF-4+ 2022 database.

Furthermore, the oxygen content of the oxide powder was measured by inert-gas fusion technique via ONH-analyzer G8 GALILEO. Approximately 0.02 g of sample per run was introduced into a Sn crucible and heated in a graphite furnace to 2200 °C. After the measurement, the droplet of Sn with the embedded remaining portions of sample was kept to confirm the completeness of oxygen removal. To collect statistics, 4-5 measurements were performed per each sample.

D. *Optical Emission Spectroscopy (OES)*

To investigate the temporal evolution of plasma and the reduction process, optical emission spectroscopy (OES) and video recording were used in a separate set of experiments with the same plasma lengths, pressures, and currents as the ones described above similarly to the previous work.[12] In these experiments, 15 g magnetite samples were compressed into cylinders and processed in 2.5 minutes steps up to 15 minutes total power-on time. The chamber was replenished with fresh mixture of Ar-10 pct H_2 after each step. A three-channel AvaSpec-ULS4096CL-EVO with a FC3-UVIR600-2-BX optical fiber from Avanes was used to acquire the optical

Table I. Chemical Composition of Magnetite Sample Used in this Study, Given in Wt Pct

Fe	Si	Al	Mn	Ti	Ca	Mg	S	P	O
Balance	0.190	0.074	0.470	0.260	0.093	0.376	0.174	0.017	27.650

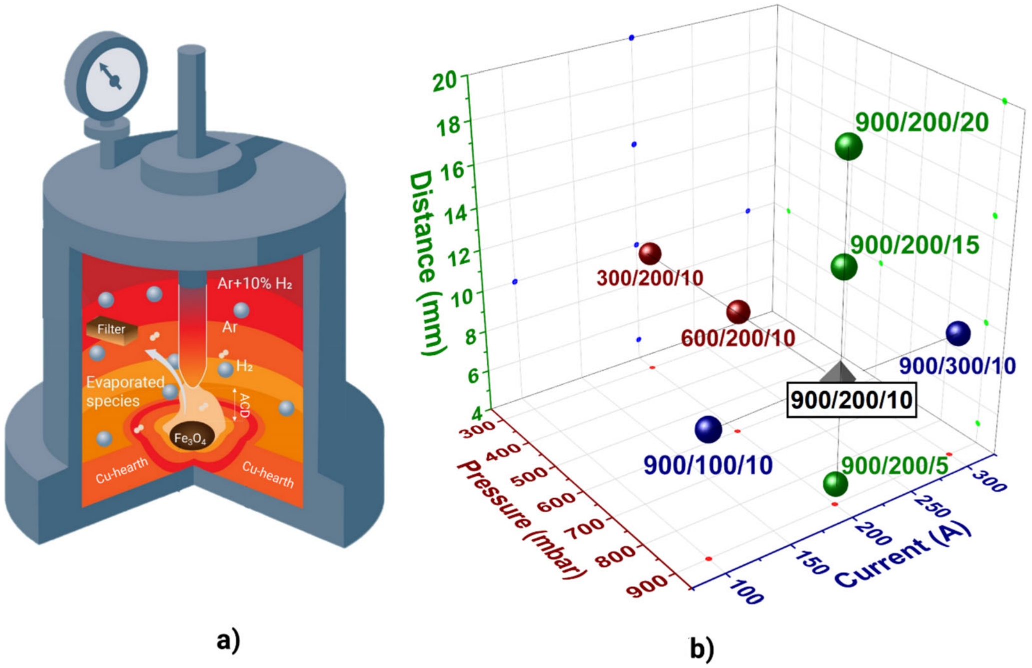

Fig. 1—(*a*) Schematic representation of the arc melting furnace used in this work. (*b*) Matrix of the varied parameters of electric arc melting furnace denoted in the "$x/y/z$" axis form, where x = pressure in mbar, y = current in A, and z = distance from electrode to the sample in mm.

spectra of plasma. The focus of this study lies in the ultraviolet (UV) and visible (VIS) spectrometers' spectra covering approximately 200–680 nm spectral range, which covers the optical emissions from majority of the species that are involved in the reduction reaction. The videos were recorded with a Canon EOS 6D single-reflex lens camera with a D5 sunfoil, essentially decreasing the light intensity to a fraction of 10^{-5}, from Teknofokus as a filter to prevent the camera from saturating from the extremely bright plasma. The values of exposure, aperture, and ISO were set to 1/80, F4.0, and 1000, respectively, and were kept constant together with white balance in all the experiments.

E. *Thermodynamic Modeling*

Equilibrium calculations were conducted using the software ThermoCalc coupled with the database TCS Metal Oxide Solutions (TCOX10) and the SSUB5 SGTE Substances database. The reduction of a 15 g molten iron oxide Fe-27.7wt pct O (Table I) was simulated by exposing the liquid to an increasing amount of a gas mixture of Ar-10 pct H_2. For these calculations, the degree of reduction is considered as "as the oxygen mass loss from the oxide liquid" (Section III–A). When considering a 15 g of molten ore (27.7 wt. pct O), the total initial mass of oxygen is 4.155 g. Therefore, the reduction degree is calculated as

$$R = \left| \frac{[O] - 4.155}{4.155} \right|,$$

where R is the reduction degree and [O] is the content of oxygen remaining in the sample.

The efficiency of hydrogen consumption during reduction was calculated at the different absolute pressures of 300, 600, and 900 mbar and at a temperature of 1850 °C. This temperature was chosen to represent the temperature estimated at the reaction interface existing between the plasma arc and the molten material.[13]

III. RESULTS AND DISCUSSION

A. *Theoretical Considerations of the Reduction Process*

Figure 2 shows the reduction path of a molten iron oxide Fe-27.7wt pct O under equilibrium conditions. In this figure, the amount of oxide and metallic liquids are plotted as a function of the reduction degree, which was calculated as the oxygen mass loss from the oxide liquid. In general, the consumption of the oxide liquid to form

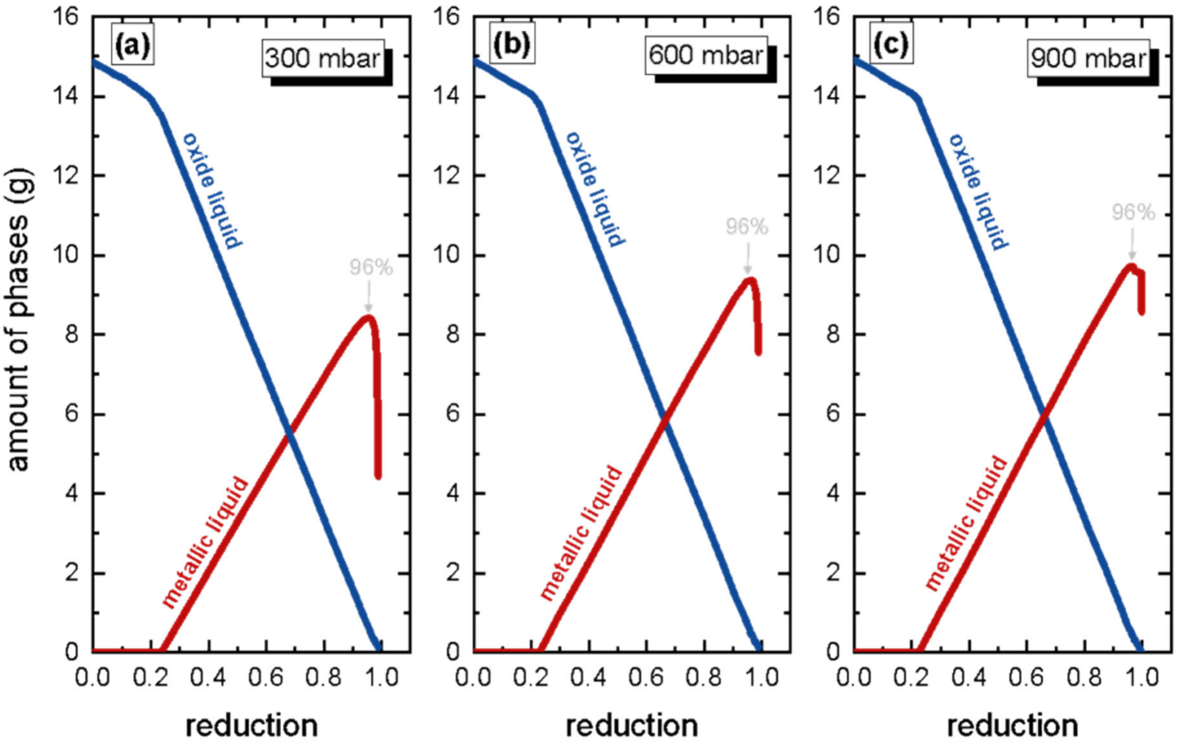

Fig. 2—Theoretical reduction of a molten iron ore (27.7 wt pct O) deliberatively exposed to increasing amounts of a gas mixture of Ar-10 pct H2 at 1850 °C. The reduction is calculated under the different absolute pressures of (*a*) 300 mbar, (*b*) 600 mbar, and (*c*) 900 mbar.

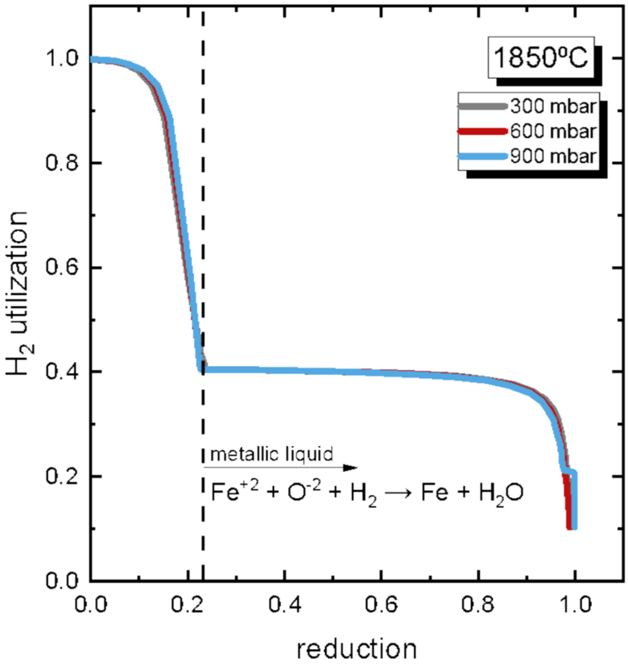

Fig. 3—Efficiency in hydrogen consumption during the reduction of a molten iron oxide (Fe-27.7 wt pct O) exposed to Ar-10 pct H2 gas mixture, at 1850 °C and 300, 600, and 900 mbar, calculated based on the theoretical mass loss of oxygen.

the metallic one has the same trend for all employed absolute pressure (300, 600, and 900 mbar). However, the absolute pressure of the system imposes an influence on the total amount of metallic iron obtained. Increasing the pressure from 300 to 900 mbar allows for improving the metallic yield, from 8.4 g to 9.7 g, respectively. These values correspond respectively to 77.4 and 89.4 pct of reduction degree. This observation suggests that lesser amounts of Fe partitions to the gaseous phase at higher absolute pressure values. Figure 2 also shows that most of the evaporation events occur after a reduction degree of 96 pct. At 300 mbar, a staggering evaporation of 46 pct of the obtained iron occurs (the amount of metallic Fe drops from 8.4 g at 96 pct reduction to 4.5 g at 100 pct reduction). Increasing the pressure to 900 mbar, the evaporation of the metallic iron drops to 11 pct.

Figure 3 shows the efficiency in H_2 utilization during reduction of the molten iron oxide (27.7 wt pct O) calculated with the aid of *ThermoCalc* software. An overall view of this figure reveals that the absolute pressure exerts little influence on the efficiency in consumption of hydrogen, which remains nearly constant at 40 pct from 22 to 80 pct reduction. Above 80 pct, the process progresses with a substantial drop until reaching 10 pct at 99 pct reduction.

B. *Reduction Kinetics and Evaporation*

The initial and final masses of the samples before and after reduction were recorded. Upon crushing, oxide and metallic fractions of the samples were separated and weighed. The XRD measurements with consecutive refinement of the separated and further powdered oxide phases allowed for the estimation of the distribution of Fe within all constituents contained in the samples after

1, 5, 10, and 15 minutes, as shown in Figure 4. In most of the experimental setups, 0.5 minute was not enough to fully melt the sample to begin reduction, therefore, this point was omitted from the presentation of phase distribution

Gradual increase in the yield of metallic phase is observed at all experimental setups from 5 to 15 cycle and, except for the case of using the lowest possible current (900/100/10), the reduction process seems to be finished after 15 minutes providing metallic yield ranging from 70 to 80 pct. It can be observed from the Fe distribution that almost in all parameter combinations, magnetite is not observed at 5 minutes reflecting the relative instability of magnetite phase. At all possible parameter combinations, the conditions are sufficient to quickly reduce almost all the magnetite to wüstite, which is present in various stoichiometries (*viz*., $Fe_{1-x}O$[14]) up to 10 minutes. The gangue elements seem to be dissolved in all of the mentioned oxidic phases and are difficult to account for in full, which might be the reason for the uneven growth of the metallic yield and the calculated losses of iron. However, if the assumed discrepancies in calculations can be considered consistent among all the experiments, one can compare the loss of metallic iron between various experiments when the system only consists of metal after the reduction (15 minutes). Such comparison is visualized in Figure 5, where only one parameter set is added with 10 minutes—900/300/10—where the metal was obtained even after 10 minutes.

The notable difference can be observed for the pressure set, where lowering of the pressure resulted in gradual increase of the loss in metallic Fe. This can be the direct consequence of increase in volatility of iron at lower pressures and elevated temperatures as predicted from P–T diagram.[15] The ACD does not have such an effect on iron evaporation, neither does the current, both exhibiting the losses on the order of 20 pct after 15 minutes of plasma exposure. Interestingly and, perhaps, the most promising result is observed for the test of higher current experiment (900/300/10), where the full metallic nugget was obtained already after 10 cycles. This allowed for the decrease in losses of iron to 12 pct instead of 20 pct due to lowering of the processing time, which is the time of material existence at evaporating conditions. Such effect could potentially be beneficial to

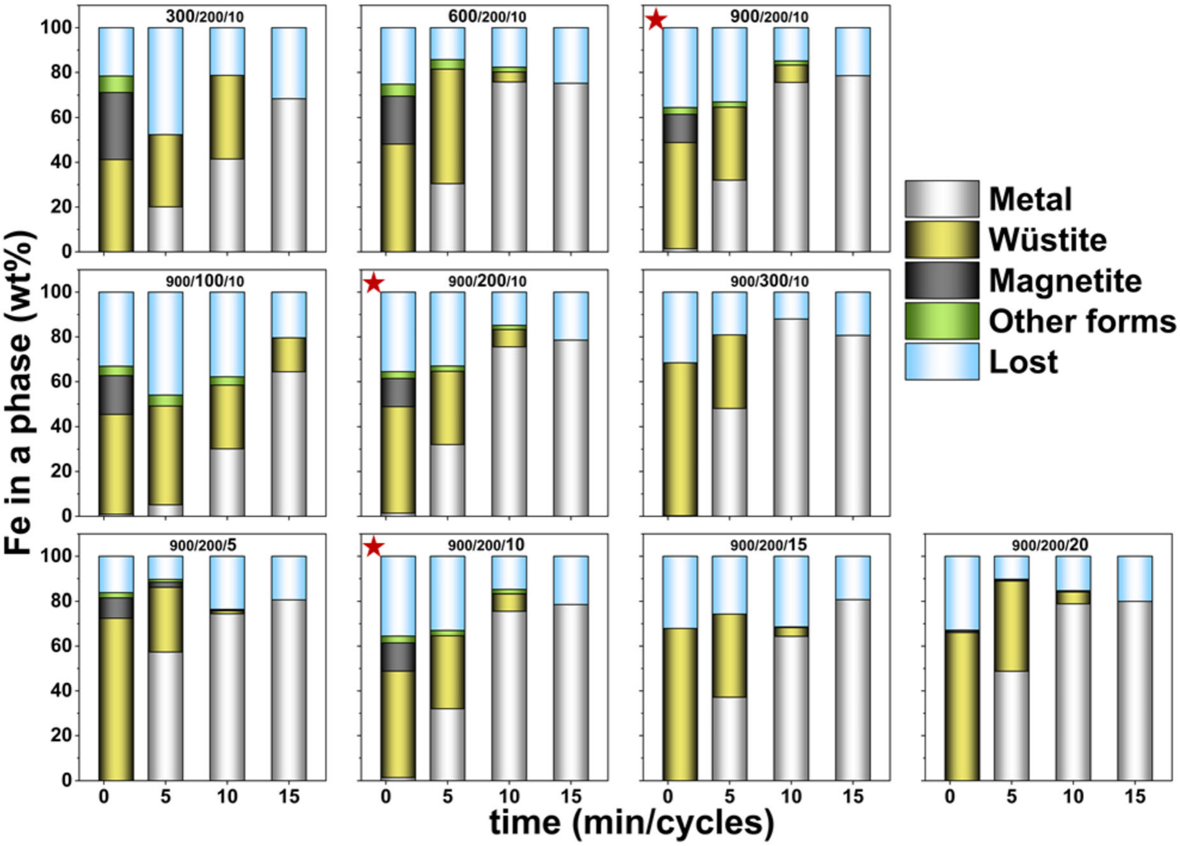

Fig. 4—Iron distribution between phases/lost during reduction process after 1, 5, 10, and 15 cycles. “Metal” represents the amount of metallic phase plus mechanically inseparable metal particles that are seen in PXRD as bcc-Fe reflections. “Wüstite” and “Magnetite” are the sums of matched $Fe_{1-x}O$ and Fe_3O_4 species with phases of other metals that can form solid solutions with the abovementioned phases (TiO_x, MgO, MnO_x). Due to the low amounts of gangue elements, they can be neglected in calculation assigning the whole phase to iron in calculations. “Other forms” is related to the silicates and other oxides that might contain Fe. “Lost” is the balanced amount of Fe that was not in metallic nor in oxide part of the sample but missing from the 15g of initial mass. The numbers in xxx/yyy/zz format represent values of pressure(mbar)/current(A)/ACD(mm). The star denotes the same experimental result duplicated for an easier comparison.

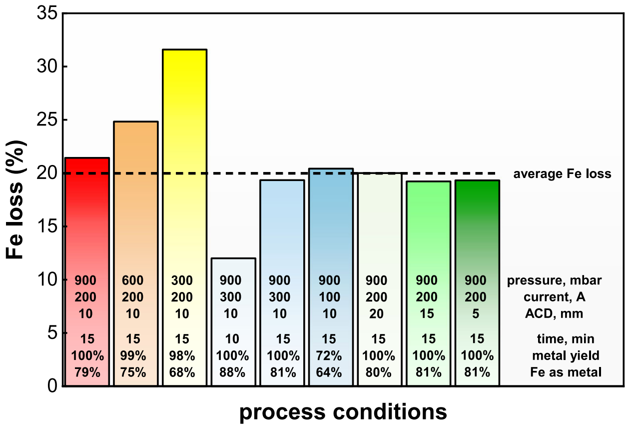

Fig. 5—Comparison of iron loses between the series of experiments.

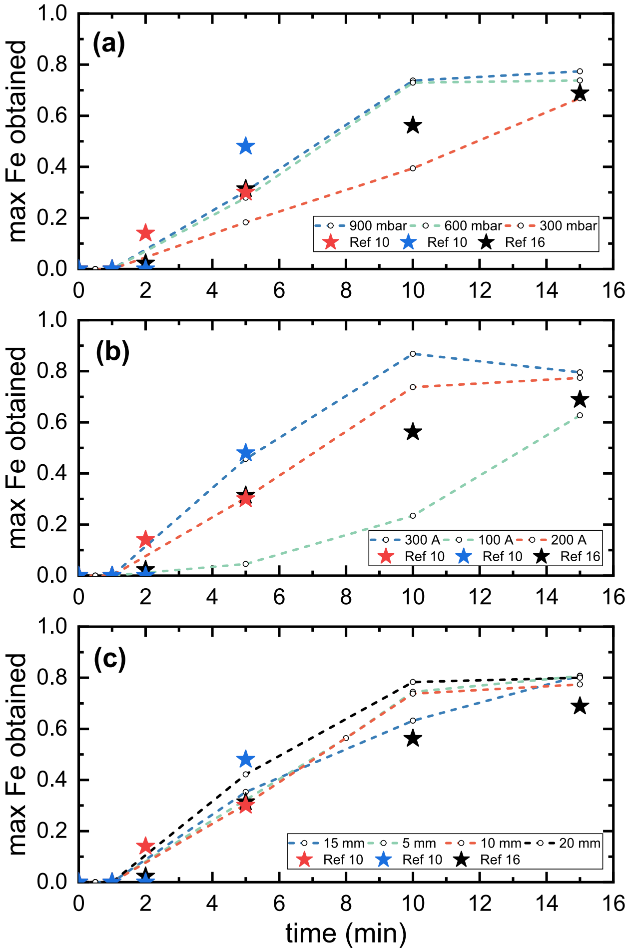

Fig. 6—Reduction kinetics in terms of the metallic Fe obtained (calculated by the ratio between the amount of metallic Fe obtained after each experiment by the total amount of Fe contained in the original 15 g sample—*viz.*, approximately 10.6 g). (*a*) Reduction kinetics for the set of experiments in which the absolute pressure values were 300, 600, and 900 mbar (the current and ACD were kept constant at 200 A and 10 mm, respectively). (*b*) Reduction kinetics for the experiments conducted at the different currents of 100, 200, and 300 A (the absolute pressure and the ACD values were kept constant at 900 mbar and 10 mm, respectively). (*c*) Reduction kinetics for the experiments conducted at 900 mbar, 200 A, and at different ACD values (5, 10, 15, and 20 mm)..

the metallurgy as it would provide the faster reaction, however, increasing the current has a direct effect onto the energetic efficiency of reduction process.

Based on the data displayed in Figures 5 and 7, one can also construct the reduction kinetics for all set of process parameters adopted in this work, as documented in Figure 6. In this figure, the metallic Fe obtained (calculated by the ratio between the amount of metallic Fe obtained after each experiment by the total amount of Fe contained in the original 15 g sample—viz., approximately 10.6 g) is plotted as a function of time (reducing cycles). These data reflect the actual metallic gain and account also for the losses via the vapor phase (Figure 5). In the same figure, the reduction kinetics for experiments reported in the literature are also plotted for comparison. The data represented by red stars in Figure 6 were obtained from[10] and represent the reduction kinetics of hematite via HPSR under a gas atmosphere of Ar20 pct H_2. The blue stars in Figure 7 represent the reduction kinetics of hematite conducted under an atmosphere of Ar-10 pct H_2 at absolute pressure of 450 mbar, as reported in.[10] The data obtained from[16] (black stars in Figure 6) represent the metallic Fe gain obtained via HPSR of a low-grade hematite ore variant containing 1 pct P.

Figure 6(a) shows the reduction kinetics for the set of experiments in which the absolute pressure was changed from 300 to 900 mbar (the current and ACD were kept constant at 200 A and 10 mm, respectively). The reduction kinetics for the experiments conducted at 600 and 900 mbar are virtually the same and a maximum of 80 pct of Fe can be recovered after 10 minutes of the process. Conducting the process at 300 mbar yields the lowest efficiency in reduction. The experiments reported in Reference 16 reveal a maximum of 70 pct of Fe gain and particularly for 5 minutes of the process, it seems that the highest yield is achieved when using 10 pct H2 and an absolute pressure of 450 mbar.

Figure 7(b) shows the reduction kinetics for the experiments conducted at different currents used to ignite the arc (the absolute pressure and the ACD values were kept constant at 900 mbar and 10 mm, respectively). The results obtained in the present work seem to be consistent with the ones reported in the literature for reduction periods of up to 5 minutes. Conducting the reduction experiments at 100 A yields the lowest Fe gain, as shown in Figure 7(b). A maximum gain of Fe (87 pct) is obtained using a current of 300 A and processing the ore for 10 minutes. Further process only leads to excess of evaporation, thus dropping the amount of obtained Fe to 80 pct, a value that is similar to the one achieved after 15 minutes of reduction at 200 A.

Finally, Figure 7(c) displays the Fe yield for experiments conducted at 900 mbar, 200 A, and at different ACD values. The lowest efficiency in Fe recovery occurs for ACD values of 15 mm, but it is still slightly more efficient than the reduction performance displayed in Reference 16. The highest Fe amount was obtained when using an ACD of 20 mm and processing the ore

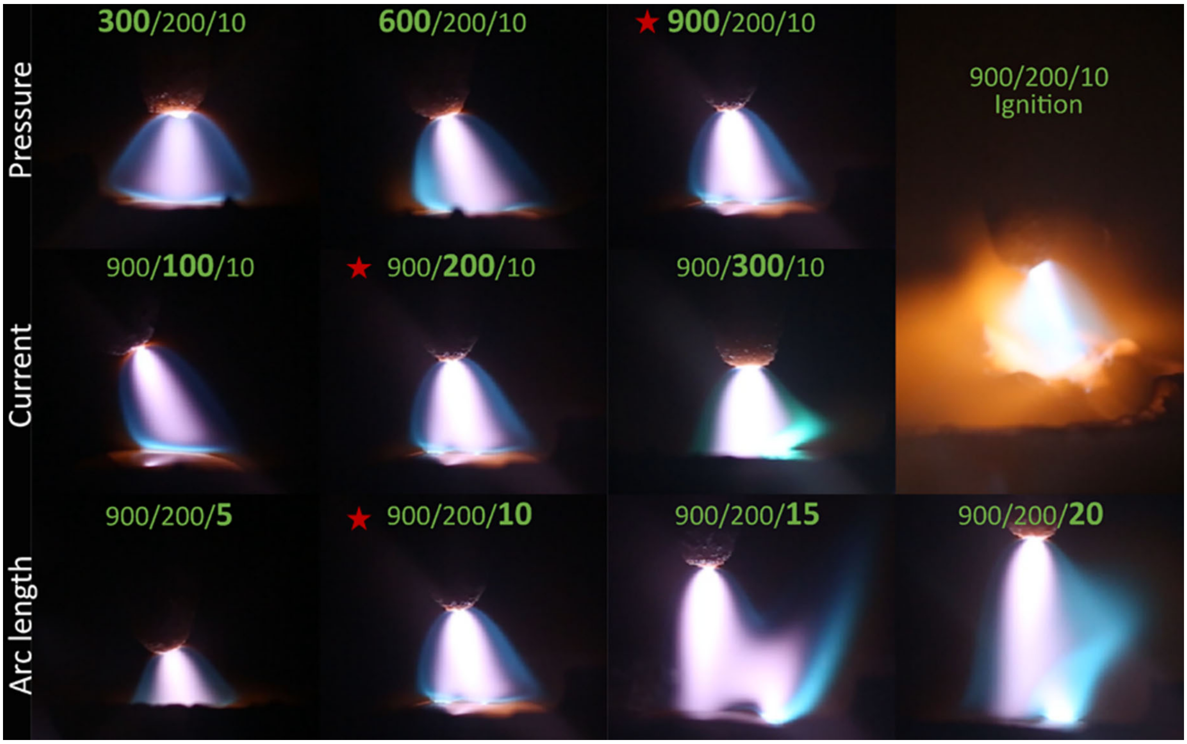

Fig. 7—Typical plasma images with different pressures, currents, and arc lengths. The numbers in xxx/yyy/zz format represent values of pressure (mbar)/current (A)/ACD (mm). The star denotes the same experimental result duplicated for an easier comparison.

for 10 minutes. Up to 5 minutes of the process, the reduction trends are similar to the results reported in References 10 and 16.

C. *Plasma Monitoring*

Recording plasma and measuring its spectral properties throughout the experiments allow for a better assessment of the effects of furnace parameters. The snapshots of the most notable plasma behavior at studied conditions are shown in Figure 7. Plasma has several distinct colors that evolve during the process: a blue sheath around it, a light-red/white body, and a bright white core. Blue and red colors correspond to the 400–500 and 600–700 nm ranges, respectively. At the ignition, a strong orange glow surrounds the plasma and can be observed in the plasma even after the ignition. After 3 minutes, the plasma stabilizes and the differences between the experiments can be seen more easily. Generally, when the gas-mix pressure is lower, the brightness of the plasma decreased and the plasma widens horizontally, thus increasing its volume. Lowering the current decreases brightness, as is expected due to a lower power. A decrease in brightness is also observed for the longer arcs.

Optical emission spectroscopy measurements were performed to characterize the colors with respect to the atomic species that radiated within the plasma. Here, the emission lines are labeled with an element symbol followed by a Roman numeral to depict both the species and the ionization degree, where I and II correspond to neutral and singly ionized atom, respectively. Three exemplary spectra are shown in Figure 8, where a) and b) showcase the UV and VIS spectra for 900/200/10 at 5 minutes. Most optical emissions originate from Fe I, Fe II, H I, Ar I, and Na I. The spectrum of light, blue, orange, and red lights correspond to wavelengths around 450-500 nm, 550-600, and 650-700 nm, respectively. The spectra show that the blue light consists of Fe I and H I, orange of Na I, and red by H I. However, the hydrogen line at 488 nm was observed not to contribute to the temporal changes in the blue light of the plasma images. Na I, on the other hand, was observed to be affected by strong self-absorption and self-reversal due to high amount of sodium in the atmosphere.

At 900 mbar and 200 A, there are clear indications when the metallic iron starts to form on the surface of the melt for 10, 15, and 20 mm experiments. Unfortunately, the melt surface for the 5 mm experiment was not visible to the camera. Bright blue glow can be observed for these three experiments where the plasma occasionally undergoes double arcing. This double arcing occurs when the main arc column goes straight to the melt, but a branching arc seeks the high-conductivity metallic iron moving on the melt. At these instances, metallic iron was observed to float to the sides of melt and sink below the oxidic melt. The double arcing is accompanied by very bright blue light from the melt, which originates from the atomic Fe I optical emission. Between 12 and 15 minutes, the double arcing is not observed anymore, and a bright blue spot is visible where the plasma hits the melt: this bright spot is metallic iron evaporating into the plasma. The origin of the colors will be discussed further in the following paragraphs.

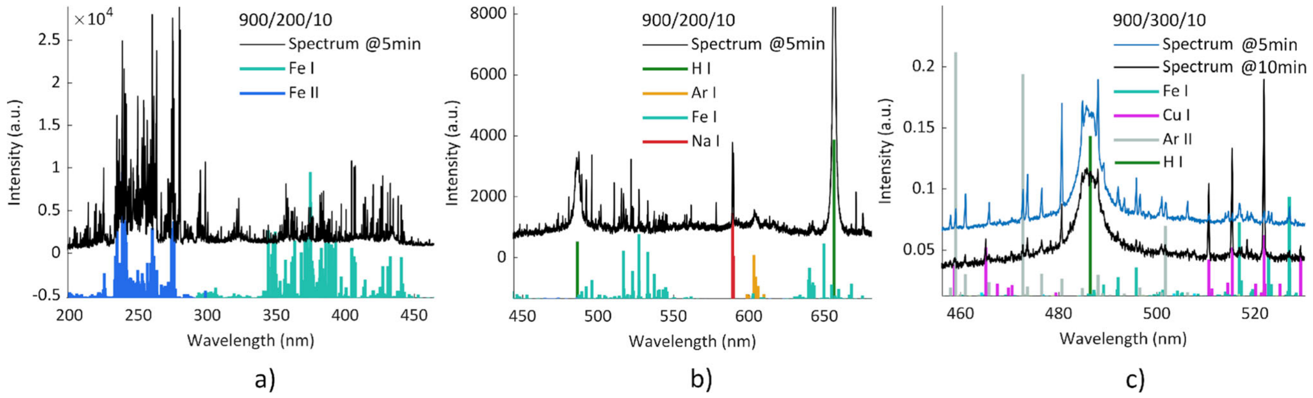

Fig. 8—Spectra from 900/200/10 experiment at 5 minutes obtained in (*a*) UV and (*b*) VIS ranges. Spectrum from 900/300/10 experiment for (*c*) VIS range. The numbers in xxx/yyy/zz format represent values of pressure (mbar)/current (A)/ACD (mm).

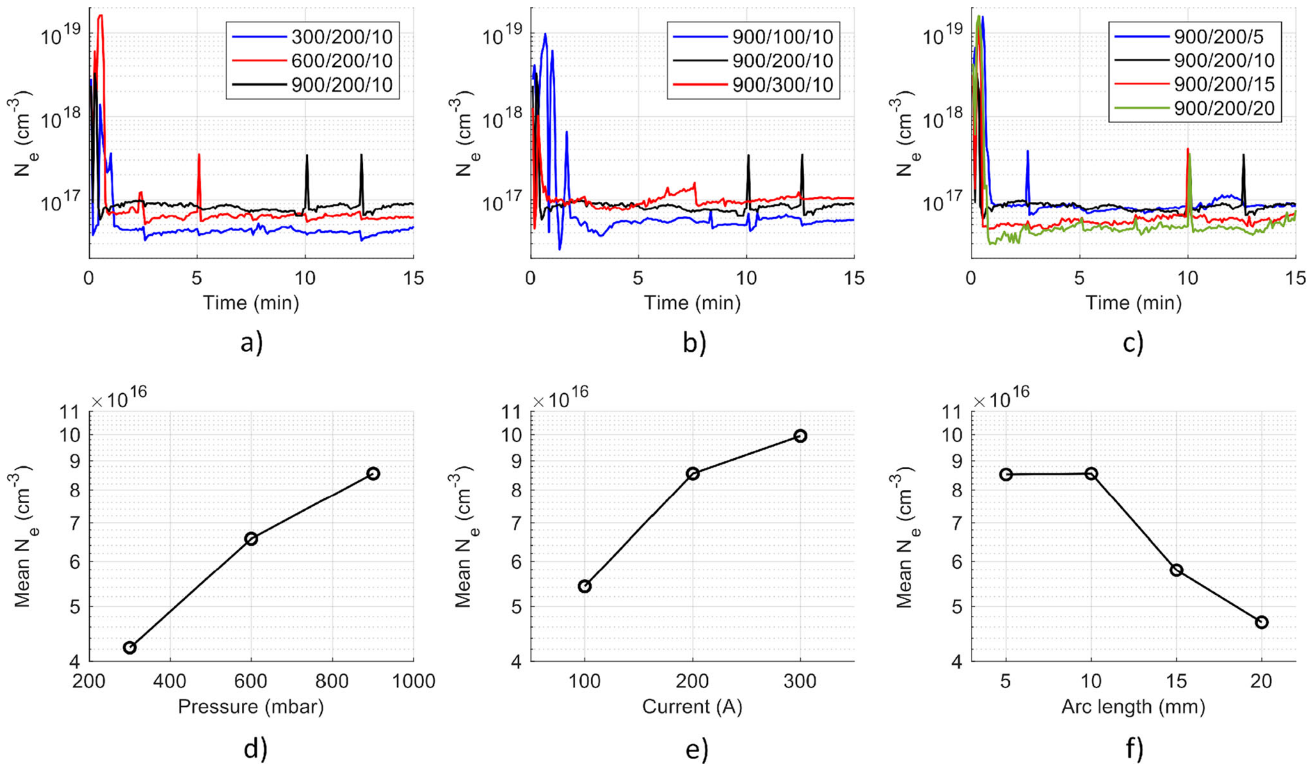

Fig. 9—Mean electron densities over 5 s for experiments (*a*) 10 300-900/200/10, (*b*) 900/100-300/, and (*c*) 900/200/5-20. The mean values after the first 1.5 minutes (i.e., when the sample had melted and plasma was stabilized in all experiments) are displayed in (*d*) to (*f*), respectively. The numbers in xxx/yyy/zz format represent values of pressure (mbar)/current (A)/ACD (mm).

Only in the 900/300/10 experiment, a green sheath can be seen around the core of the plasma in Figure 7. Figure 8(c) shows two spectra for this experiment at 5 and 10 minutes, revealing that the green light originates from Cu I optical emissions between 510 and 522 nm. In addition, some of the optical emissions from ionized argon can be seen at this wavelength range. Since the only source of copper is the crucible, it was concluded that the crucible started to partially melt and mix with the sample despite the water cooling. The 900/300/10 also showed the least amount of Fe I and blue light from 5 minutes onward, which is most probably caused by the emerging copper. In addition, the sample welded into the crucible between the experimental steps due to the high power. This means that the 900/300/10 experiment should not directly be compared to, *e.g.,* the results of iron distribution analysis shown in Figure 4.

Plasma can further be characterized by deriving the electron density and plasma temperature with the same methods as in previous publication.[17] The temporal evolution of electron density (N_e) is shown in Figure 9 for all the experiments in (a) through (c) together with the mean values over 5 s from 1.5 minutes onward in (d) through (f). Electron density reaches the highest values during the first 1-1.5 minutes of the process, reaching relatively stable values after this. A few higher spikes can be observed in some experiments during the arc ignition in the beginning of the 2.5 minutes step. The electron densities in 900/200/5 and 900/200/10 are relatively close to each other but increasing the arc length to 15 and 20 mm decreases the electron density due to an increase in the plasma volume. As was observed earlier, lower pressure increases the plasma volume, which is consistent with lower electron densities for 300 and 600 mbar in comparison with 900 mbar. Higher current induces higher electron density due to stronger ionization of species, but the emerging copper might influence the 900/300/10 when compared to the other experiments.

The plasma temperature was determined with Fe I optical emissions to assess the effect of metallic vapor (Figure 10). It was found out that the sudden increases in Fe I, which correspond to the blue flashes near the melt and within the plasma, tend to decrease the plasma temperature. This observation is to be expected, since it has been demonstrated that metallic vapor cools down the plasma due to, *e.g.,* high radiative energy transfer.[18,19] On the other hand, during stable periods where there are no spikes in Fe I intensity nor blue flashes, these trends are not present. When Fe I intensity is higher than 2-10 × 10^4 (in arbitrary units), the trends follow a reverse relation [Fe T] ~ 1 / [Fe I]. The trends of the relation are clear, even though most of the data are scattered around the fit curve. The distribution of temperatures shown in Figure 10 allows for the estimation of plasma homogeneity. It can be observed that for most sets of parameters, the distribution of temperatures is composed out of the 1 or 2 peak positions. Since Fe I can be observed as a blue sheath around the plasma, it is assumed that the temperature describes the sheath regions of the plasma rather than the plasma column or the core.

Figures 11(a) through (c) show the temporal evolution of Fe I and the observed ionic species Fe II and Ar II to better understand how these species evolve during the experiments. The spikes in Fe I and Fe II after 7.5-10 minutes in the 900/200/5-10-15-20 experiments correspond to the formation of metallic iron on the melt and the double-arcing phenomenon. The 300-600/200/10 show elevated values of Fe I and Fe II in comparison to 900/200/10, which can be caused by higher evaporation rate of iron into the plasma in lower pressures. The trends start to decline for the 900/300/10 after 5 minutes, when the copper started to dominate the color of the plasma.

The Ar II optical emissions are relatively similar in 900/200/5-10 but seem to decrease with increasing arc length. The lowest Ar II emissions are observed with the highest arc length (900/200/20) and the lowest current (900/100/10). Also, the Ar II intensity drops after 5

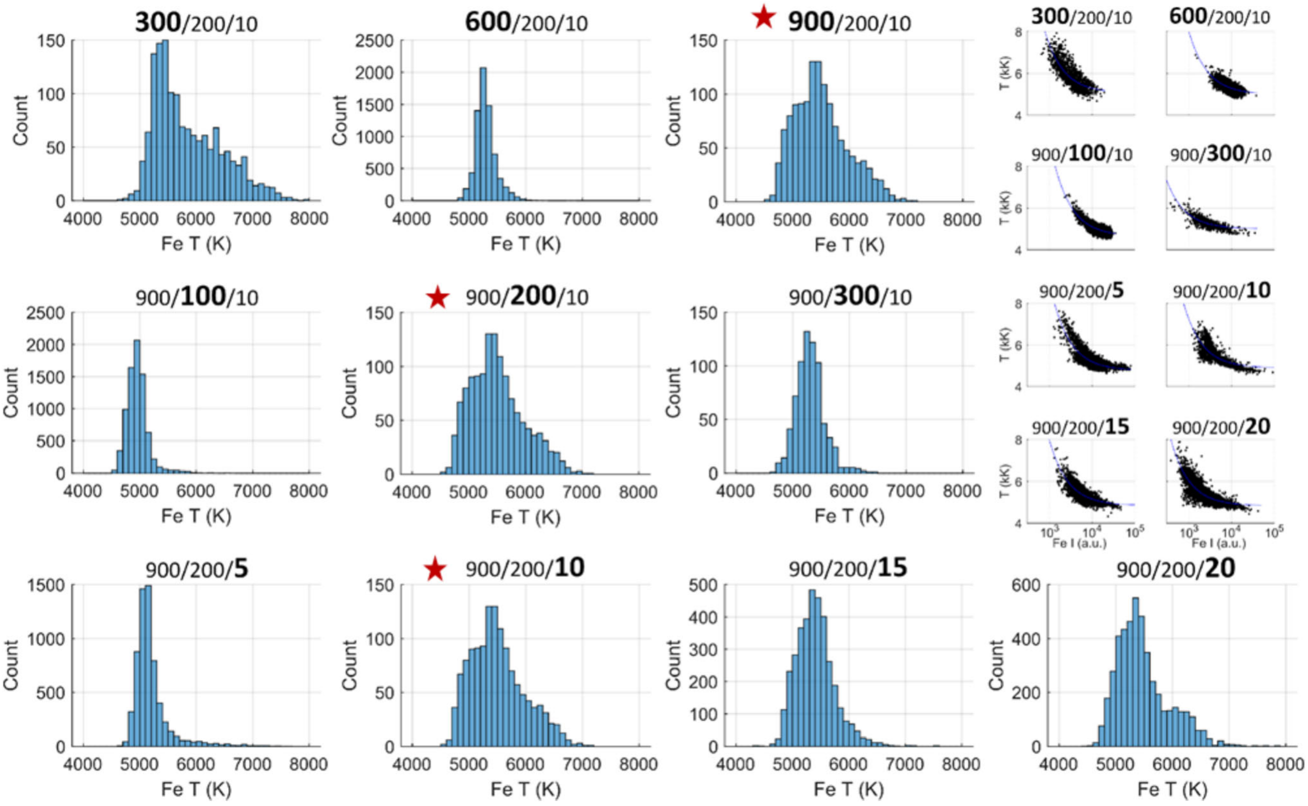

Fig. 10—Plasma temperature distribution in 100 K steps with the actual data in reduced inserts. Only temperatures with Boltzmann plot's R^2 higher than 0.85 were considered for these plots. The numbers in xxx/yyy/zz format represent values of pressure (mbar)/current (A)/ACD (mm). The star denotes the same experimental result duplicated for an easier comparison.

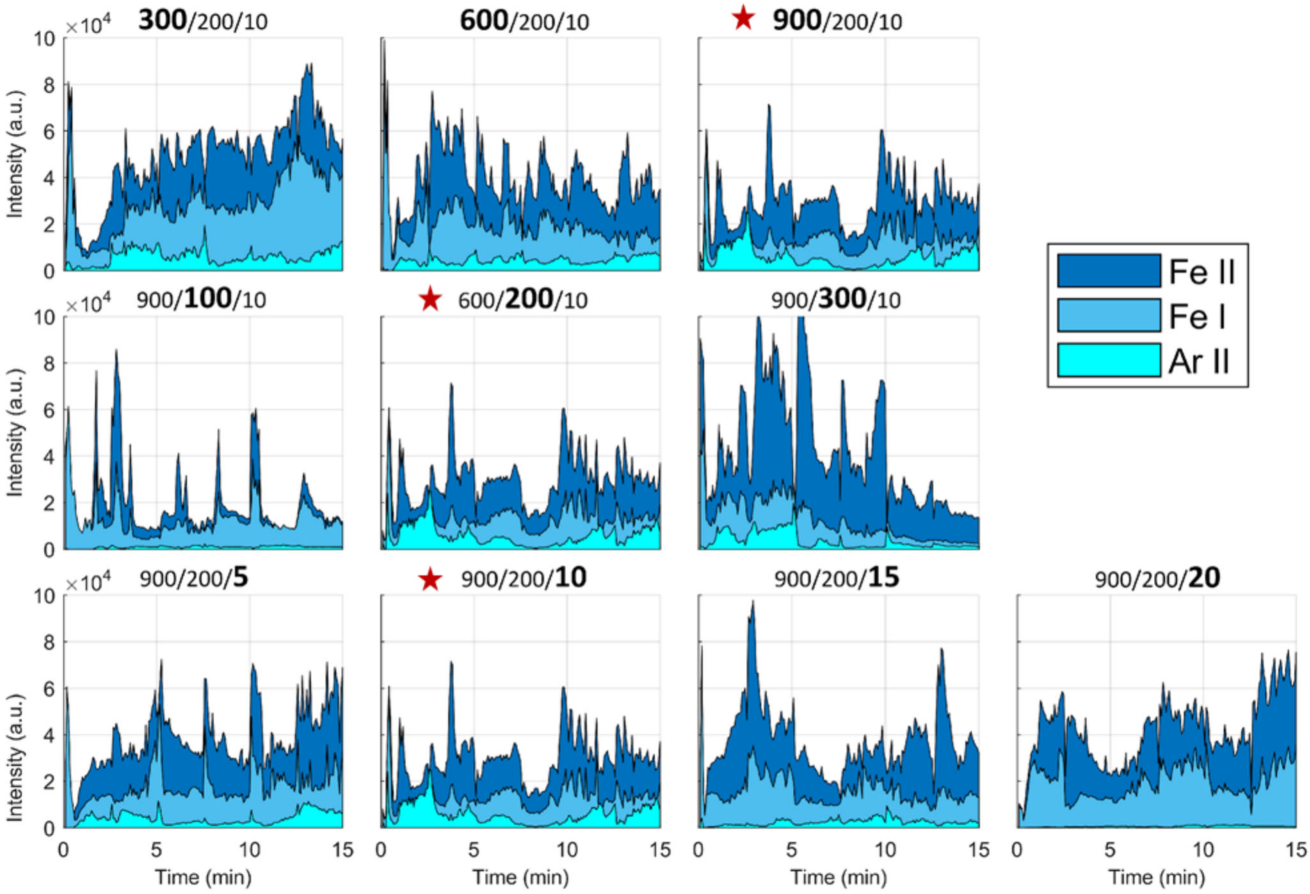

Fig. 11—Temporal evolution of Fe I, Fe II, and Ar II for all the experiments. The values are means of 5 s. The numbers in xxx/yyy/zz format represent values of pressure (mbar)/current (A)/ACD (mm). The star denotes the same experimental result duplicated for an easier comparison.

minutes for the 900/300/10, which could mean that the copper in the plasma has a cooling effect to the plasma temperature.

One of the most interesting major components in the reduction reaction, and the optical spectra, is of course hydrogen. Since the 90 pct Ar/10 pct H_2 gas mix is introduced into the reactor at the very beginning of the experimental steps, it can be expected that H_2 is atomized, ionized, and eventually partly or totally consumed to the reduction reaction, forming water vapor. The temporal evolution of H_β/Ar I intensity ratio is shown in Figure 12 for all the experiments.

The intensity of H_β was divided by the intensity of Ar because the content of Ar can be estimated as a constant during the process despite the movement of the arc by manual electrode movement. Then hydrogen usage was estimated from the OES spectra by tracking the decreasing trend of the H_β/Ar I intensity ratio. Essentially, the lower the intensity ratio, the higher the H_2 utilization. Since the calculated H_2 utilizations during the first minute of reduction are close to 100 pct for the experiments, it was assumed that the OES-based H_2 utilization is 100 pct for the first 2.5 minutes of experimental step. The sequential experimental steps were then scaled with this value. Both the calculated and the OES-based H_2 utilizations shown in Figure 12 exhibit similar trends.

D. *Energetic Efficiency of Reduction*

The effectiveness of the metallization comes not only from the metal yield as it is, but also from the energy used throughout the experiment. Firstly, it is reasonable to look at the total energy consumption per set of experiments by summing up data from all 31.5 minutes of exposure of magnetite sample to the plasma arc. Thus, the energy consumption was recorded for each sample set and then summed up to provide the initial picture of how the arc melting reactor's parameters would affect it. The slight mass variation between the samples can be neglected.

Figure 13 illustrates the variations in energy consumption observed across different experimental parameters, highlighting contrasting trends. The most significant variation is seen in experiments involving changes in current, a direct consequence of current's strong influence on voltage and its critical role in modulating plasma temperature. These results affirm the primary dependence of energy consumption on current, as the plasma conditions are most directly altered by this parameter.

In contrast, both "Pressure" and "Distance" sets exhibit saturation trends. Specifically, energy consumption saturates between 600–900 mbar for pressure and 5–15 mm for distance. Notably, lower distances between

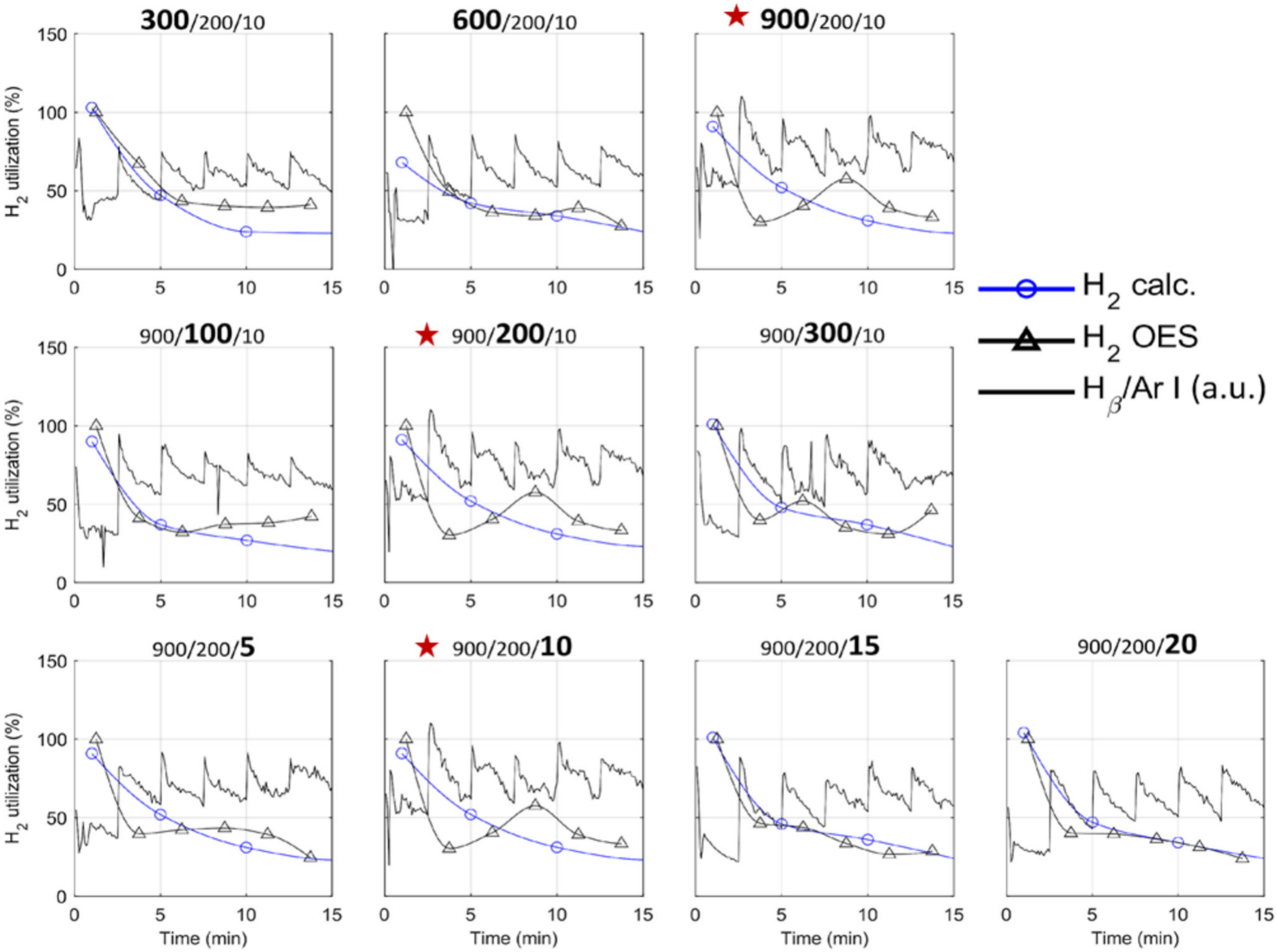

Fig. 12—Mean Hβ/Ar I intensities over 5s together with calculated and OES-based H2 utilization in percentages. The OES-based values are displayed at the mid-point of each experimental 2.5 minutes steps. The numbers in xxx/yyy/zz format represent values of pressure.

the electrode and the sample were expected to reduce energy consumption, but this trend was not observed in our study. This anomaly may be attributed to a threshold effect in plasma plume formation under the given pressure and current conditions. For example, at 900 mbar, experiments (900/200/zz) reveal a comparable width and brightness in the plasma sheath and body, whereas at lower pressures, such as 300 mbar (xxx/200/10), the plume contracts and intensifies, becoming paler. Similarly, at higher currents (*e.g.,* 300 A in 900/yyy/10), the plasma plume appears more pronounced compared to the paler plume at 100 A. These variations align with the findings in welding arc studies, which emphasize the critical roles of pressure and current in plume formation.[20]

Beyond 15 mm, an increase in distance necessitates higher voltages to sustain the arc, leading to increased energy consumption. For pressure, variations can be attributed to the dielectric constants of the gases used in the experiments; lower pressures generally require less power to sustain the arc due to reduced resistance to electrical discharge.[21]

To elucidate further the energy consumption, the sets of experiments were assessed individually. Given the abovementioned relatively low dependency of energy consumption between the sets of experiments, the degree of reduction is the major accountant for the following discussion. For this reason, all the obtained results on metal yield were normalized per energy consumed at each experiment and plotted in Figure 14. In this figure, the normalized metallization is calculated as the ratio of the amount of metallic iron with respect to initial oxide (i.e., degree of metallization) to the total energy input for each experiment. This metric serves as an indicator of energy efficiency in the reduction process.

It is notable that the efficiency of iron reduction per unit energy greatly increases when it is conducted at 600 *vs.* 300 mbar, but then does not change much between 600 and 900 mbar, meaning the saturation of this trend. Similar effect can be seen for the effect of ACD onto the system. At longer distances (15 and 20 mm), the efficiency is lower compared to shorter arcs of 5 and 10mm, however, the lowest arc can be tricky to achieve due to the unevenness of the material surface that might lead to the contact with the electrode on the industrial scale, resulting in unwanted extinguishing of the arc and

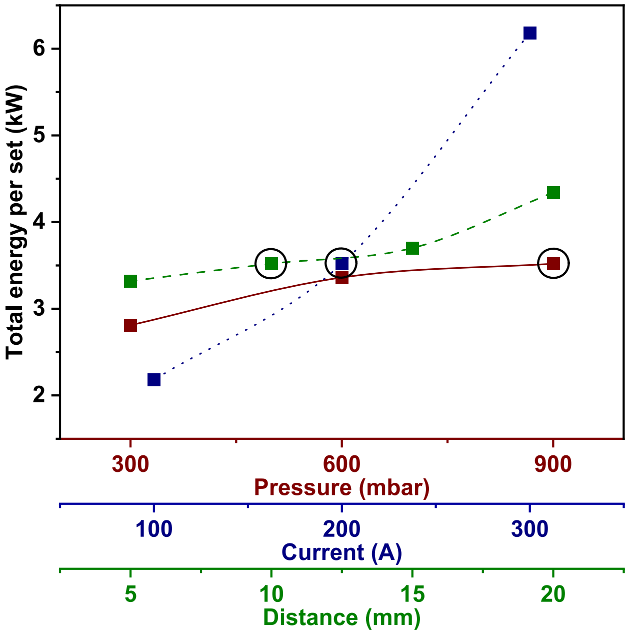

Fig. 13—Total amount of energy consumed per each set of experiments. Each point represents a sum from all measurements within one dataset. The circled data points represent the same data point (900/200/10) that overlaps between all three sets. The numbers in xxx/yyy/zz format represent values of pressure (mbar)/current (A)/ACD (mm).

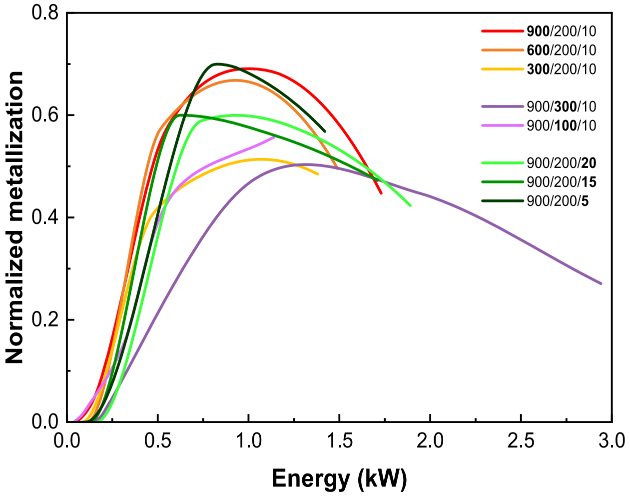

Fig. 14—Normalized metallization yield as a function of the energy consumed. The numbers in xxx/yyy/zz format represent values of pressure (mbar)/current (A)/ACD (mm).

thus affecting the reduction process. The surprising trend is observed for the current changing set of experiment, where it seems that the process has a maximum efficiency at 200 A, while 100 A leads to weak and slow reduction, and 300 A results in a fast but more energy-consuming process, so the overall most promising parameters of the current setup seem to be 900 mbar of gas pressure, 200 A of current, and 10 mm of ACD.

Although the present work focuses on laboratory-scale reduction of magnetite using hydrogen thermal plasma, the broader objective of this research lies in supporting the development of scalable and energy-efficient metallurgical processes. In contrast to hydrogen-based direct reduction routes, such as those conducted in shaft furnaces or in hydrogen-enriched blast furnaces, hydrogen plasma systems are still in early stages of development, and their industrial applicability has not yet been fully demonstrated.

Several challenges remain before the process can be translated to industrial scale. These include the need for robust plasma systems capable of stable long-term operation, improved reactor designs that ensure uniform energy distribution across larger surfaces, and effective mitigation of heat losses in larger setups, to name a few. Additionally, the aggressive nature of hydrogen plasma imposes constraints on the choice of construction materials, especially the refractory lining, thus demanding attention to reactor durability.[22] Reliable control strategies—potentially involving real-time plasma diagnostics[12]—will also be essential to regulate the reduction extent and optimize energy use during continuous operation.

Another important aspect to be considered in scaling up is the stabilization of arcs ignited at a few hundred kA[17] and the accompanying possible interference with the mass transfer of hydrogen species between the plasma volume and the melt. In the present work, it is not expected that hydrogen mass transfer is the primary rate-limiting step, especially at the lower currents and stable arc conditions employed here. However, factors such as available surface area of the oxide, plasma residence time, the ratio of "power to input mass," and heat flux dominate the kinetics.[6,23] Therefore, in a scaled-up reactor operating with large currents and a mobile arc, local depletion or inconsistent delivery of reactive hydrogen species might emerge as a critical factor. This suggests that future studies should incorporate time-resolved diagnostics and modeling to evaluate the impact of arc fluctuations on hydrogen mass transfer and reduction efficiency in industrial-scale setups.

Despite these technical barriers, the hydrogen plasma approach offers unique opportunities and is already being explored at pilot scale under the initiative of K1-MET in Austria. Its high reaction rates, suitability for fine-grained or low-grade feedstocks (which can be introduced directly into the plasma zone via hollow electrodes), and compatibility with renewable electricity sources make it particularly attractive for decentralized or modular installations. In such compact and flexible setups, the full potential of HPSR's tunability—like pulling puppet strings to choreograph the interplay between power input, plasma shape, and reduction behavior—can be leveraged to respond to dynamic operating conditions.

These installations could be deployed closer to mine sites, scrap processing centers, or renewable energy hubs, reducing the need for extensive logistics infrastructure and enabling on-demand production of reduced iron. Compared to large, centralized DRI plants that require stable, high-volume feedstock and gas supply, modular plasma-based units can be scaled down and potentially operated intermittently to match variable renewable power availability. For example, containerized plasma reactors have been proposed for remote or off-grid applications in metallurgy and materials recycling, where flexibility and compactness are essential. The inherent ability of non-thermal plasmas to initiate chemical reactions without the need for high external bulk temperatures further supports process intensification in small footprints.

In this context, hydrogen plasma reactors could serve as regionally distributed nodes within a larger decarbonized metallurgical network—processing low-grade ores, filter dusts, or recycling fines that would otherwise be unsuitable for conventional shaft furnace-based DRI routes. While the current lab-scale setup handles only gram-scale batches,[6,16,22] pilot-scale systems with capacities in the range of 10–100 kg/h represent the next logical milestone toward validating this modular and flexible process model. Ultimately, these developments will help clarify the economic and technical feasibility of hydrogen plasma reduction, not only as a complement to established hydrogen-based DRI technologies, but potentially as a standalone solution for specific feedstock types or infrastructure settings.

IV. CONCLUSION

This study has systematically explored the reduction of molten iron oxide using a plasma arc reactor, focusing on understanding the interplay of pressure, current, and arc length (ACD) with process efficiency, metal yield, and energy consumption. The results highlight that the optimal conditions for maximizing metallic yield and energy efficiency involve a gas pressure of 900 mbar, a current of 200 A, and an ACD of 10 mm. Under these parameters, the process achieves high metallization rates with reduced energy demand, while mitigating the evaporation losses of metallic iron. This demonstrates the potential for fine-tuning plasma reactor operations—adjusting each control parameter like a puppet string—to achieve both high throughput and cost-effective production.

Key findings include the significant effect of pressure on the reduction degree and iron evaporation, with pressures beyond 600 mbar stabilizing the process without substantial gains in energy efficiency. The current of 200 A emerges as the most balanced operational setting, enabling rapid reduction while avoiding the excessive energy consumption seen at 300 A. Similarly, shorter ACDs yield greater efficiency but may pose operational challenges at an industrial scale, such as maintaining consistent electrode-sample spacing to avoid disruptions in the plasma arc.

Scaling up this process presents promising opportunities for industrial applications. The insights into double-arcing phenomena and material-specific interactions, such as crucible contamination, underscore the need for careful selection of reactor materials and design adjustments for continuous operation. Additionally, the demonstrated ability to maintain high H_2 utilization rates suggests the potential for integrating this process into green steelmaking strategies, utilizing renewable hydrogen sources to reduce carbon emissions.

Future work should focus on refining reactor designs to address challenges observed in this study, such as ensuring stable plasma behavior and minimizing contamination from reactor components. Moreover, pilot-scale trials are necessary to evaluate the scalability of these parameters and assess long-term operational stability, paving the way for industrial deployment of this efficient and adaptable plasma-based reduction process.

ACKNOWLEDGMENTS

Dr. Shelyug greatly appreciates the opportunity provided by Alexander von Humboldt Foundation for funding the research stay at Max-Planck Institute for Sustainable Materials and Dierk Raabe for hosting as Henriette Hertz scout. Dr. Pauna acknowledges the Horizon Europe for the H2PlasmaRed project no. 101138228, the Research Council of Finland (Academy of Finland) for post-doctoral researcher grant no. 349402, and the Steel and Metal Producers' Fund for travel grant no. 3831. The authors greatly appreciate the fruitful discussions with Dierk Raabe during the experiments planning and results analysis. The authors would like to thank the staff of Max-Planck Institute for Sustainable Materials, i.e., Michael Kulse and Dennis Klapproth for operating the arc furnace, Ubaid Manzoor for sample preparation, and Benjamin Breitbach for the PXRD measurements and analyses.

AUTHOR CONTRIBUTIONS

Anna Shelyug and Henri Pauna: data curation, formal analysis, investigation, methodology, validation, visualization, writing—original draft, and writing—review and editing; Hauke Springer: Writing—review and editing; Isnaldi Rodrigues de Souza Filho: conceptualization, methodology, project administration, resources, supervision, and writing—review and editing.

CONFLICT OF INTEREST

The authors declare that they have no known competing financial interests or personal relationships that could have appeared to influence the work reported in this paper.

FUNDING

Open Access funding enabled and organized by Projekt DEAL.

OPEN ACCESS

REFERENCES

1. C. Fleuriault, J.D. Steenkamp, D. Gregurek, J.F. White, Q.G. Reynolds, P.J. Mackey, S.A.C. Hockaday, *Advances in Pyrometallurgy* (Eds.: C. Fleuriault, J.D. Steenkamp, D. Gregurek, J.F. White, Q.G. Reynolds, P.J. Mackey, S.A.C. Hockaday), Springer Nature Switzerland, Cham 2023, https://doi.org/10.1007/978-3-031-22634-2.
2. J. Tang, M. Chu, F. Li, C. Feng, Z. Liu, and Y. Zhou: *Int. J. Miner. Metall. Mater.*, 2020, vol. 27, p. 713. https://doi.org/10.1007/s12613-020-2021-4.
3. X. Anjun, Q. Ying, and X. Kuangdi: *The ECPH Encyclopedia of Mining and Metallurgy*, Springer, Singapore, 2023, pp. 1–1.
4. R.R. Wang, Y.Q. Zhao, A. Babich, D. Senk, and X.Y. Fan: *J. Clean. Prod.*, 2021, vol. 329, p. 129797. https://doi.org/10.1016/j.jclepro.2021.129797.
5. K.C. Sabat, P. Rajput, R.K. Paramguru, B. Bhoi, and B.K. Mishra: *Plasma Chem. Plasma Process.*, 2014, vol. 34, p. 1. https://doi.org/10.1007/s11090-013-9484-2.
6. I.R. SouzaFilho, Y. Ma, M. Kulse, D. Ponge, B. Gault, H. Springer, and D. Raabe: *Acta Mater.*, 2021, vol. 213, p. 116971.
7. IEA 2022, https://www.iea.org/reports/achieving-net-zero-heavy-industry-sectors-in-g7-members, License: CC BY 4.0.
8. H. Springer, I.R. Souza Filho, L. Choisez, M.A. Zarl, C. Quick, A. Horn, and J. Schenk: *Sustain. Mater. Technol.*, 2024, vol. 39, p. e00785. https://doi.org/10.1016/j.susmat.2023.e00785.
9. D. Ernst, M.A. Zarl, M.A. Farkas, and J. Schenk: *Steel Res. Int.*, 2023, vol. 94, p. 2200818. https://doi.org/10.1002/srin.202200818.
10. I.R. Souza Filho, Y. Ma, D. Raabe, and H. Springer: *JOM*, 2023, vol. 75, p. 2274. https://doi.org/10.1007/s11837-023-05829-z.
11. K.C. Sabat and A.B. Murphy: *Metall. Mater. Trans. B*, 2017, vol. 48B, p. 1561. https://doi.org/10.1007/s11663-017-0957-1.
12. H.-R. Putaala, H. Pauna, A. Javed, U. Manzoor, D. Klapproth, I.R. Souza Filho, V.-V. Visuri, A. Ganguly, M. Huttula, T. Fabritius, and D. Raabe: *Metall. Mater. Trans. B*, 2025, https://doi.org/10.1007/s11663-025-03552-5.
13. M. Jovičević-Klug, I.R. Souza Filho, H. Springer, C. Adam, and D. Raabe: *Nature*, 2024, vol. 625, p. 703. https://doi.org/10.1038/s41586-023-06901-z.
14. Z. Liang, K. Li, J. Zhang, and A.N. Conejo: *NPJ Comput. Mater.*, 2025, vol. 11, p. 32. https://doi.org/10.1038/s41524-025-01527-3.
15. W.G. Moffatt, G.W. Pearsall, and J. Wulff: *Structure and Properties of Materials. Vol I: Structure*, vol. 1, Wiley, New York, 1964.
16. Ö.K. Büyükuslu, L.S. Aota, D. Raabe, H. Springer, and I.R. Souza Filho: *Acta Mater.*, 2024, https://doi.org/10.1016/j.actamat.2024.120221.
17. H. Pauna, D. Ernst, M. Zarl, I.R. Souza Filho, M. Kulse, Ö. Büyükuslu, M. Jovičević-Klug, H. Springer, M. Huttula, J. Schenk, T. Fabritius, and D. Raabe: *Steel Res. Int*., 2024, vol. 95, p. 240008. https://doi.org/10.1002/srin.202400028.
18. A.B. Murphy: *J. Phys. D*, 2013, vol. 46, p. 224004. https://doi.org/10.1088/0022-3727/46/22/224004.
19. A. Gleizes and Y. Cressault: *Plasma Chem. Plasma Process.*, 2017, vol. 37, p. 581. https://doi.org/10.1007/s11090-016-9761-y.
20. B. Wang, X.-M. Zhu, H.-C. Zhang, H.-T. Zhang, and J.-C. Feng: *Metals (Basel)*, 2018, vol. 8, p. 512. https://doi.org/10.3390/met8070512.
21. U. Kogelschatz, B. Eliasson, and W. Egli: *Le J. Phys. IV*, 1997, vol. 07, p. C4. https://doi.org/10.1051/jp4:1997405.
22. I.R. Souza Filho, H. Springer, Y. Ma, A. Mahajan, C.C. da Silva, M. Kulse, and D. Raabe: *J.Clean. Prod.*, 2022, vol. 340, p. 130805. https://doi.org/10.1016/j.jclepro.2022.130805.
23. K. Kamiya, N. Kitahara, I. Morinaka, K. Sakuraya, M. Ozawa, and M. Tanaka: *Trans. Iron Steel Inst. Japan*, 1984, vol. 24, p. 7. https://doi.org/10.2355/isijinternational1966.24.7.